

# Kurtosis-limited Sphere Shaping for Nonlinear Interference Noise Reduction in Optical Channels

Yunus Can Gültekin, *Member, IEEE*, Alex Alvarado, *Senior Member, IEEE* Olga Vassilieva, *Senior Member, IEEE*, Inwoong Kim, *Senior Member, IEEE*, Paparao Palacharla, *Senior Member, IEEE*, Chigo M. Okonkwo, *Senior Member, IEEE* and Frans M. J. Willems, *Life Fellow, IEEE*,

**Abstract**—Nonlinear interference (NLI) generated during the propagation of an optical waveform through the fiber depends on the fourth order standardized moment of the channel input distribution, also known as kurtosis. Probabilistically-shaped inputs optimized for the linear Gaussian channel have a Gaussian-like distribution with high kurtosis. For optical channels, this leads to an increase in NLI power and consequently, a decrease in effective signal-to-noise ratio (SNR). In this work, we propose kurtosis-limited enumerative sphere shaping (K-ESS) as an algorithm to generate low-kurtosis shaped inputs. Numerical simulations demonstrate that with K-ESS, it is possible to increase the effective SNRs by 0.4 dB in a single-span single-channel scenario at 400 Gbit/s. K-ESS offers also a twofold decrease in frame error rate with respect to Gaussian-channel-optimal sphere shaping.

**Index Terms**—Probabilistic shaping, amplitude shaping, kurtosis, nonlinear interference.

## I. INTRODUCTION

THE capacity of the linear additive white Gaussian noise (AWGN) channel can be achieved by transmitting independent and identically distributed Gaussian inputs [1, Ch. 9]. Recently, probabilistic amplitude shaping (PAS) was proposed as a coded modulation strategy that achieves this capacity [2]. PAS combines an outer amplitude shaper with an inner channel encoder. The amplitude shaper selects the amplitudes of the inputs while the encoder selects their signs. For the AWGN channel, amplitude shapers are designed such that the resulting input distribution has a Gaussian-like behavior [3]–[7]. Motivated by the performance improvements obtained for the AWGN channel, PAS has attracted considerable attention in optical communication systems. It was demonstrated both numerically and experimentally that PAS with AWGN-optimal shapers provides significant gains in reach or in data rate for long-haul optical links [8]–[13].

The propagation of the optical field through the fiber is subject to nonlinearities. Its propagation is governed by the

nonlinear Schrödinger equation. Often, detection schemes designed for linear channels are used for optical communications, and hence, the nonlinear interference (NLI) is implicitly treated as noise. The so-called Gaussian noise (GN) model approximately describes the statistic of this NLI independently of the modulation format and its probability distribution [14]. This approach has been shown to be inaccurate, especially for short links, and thus, the enhanced GN (EGN) model was later proposed in [15]–[17]. The EGN model predicts that the fourth order standardized moment (i.e., the *kurtosis*) of the input distribution affects the amount of NLI: inputs with higher kurtosis lead to higher NLI, and hence, lower effective signal-to-noise ratios (SNRs) [8, Sec. IV-E1].

PAS framework was considered for long-haul optical communications for the first time in [18]. However, only the Maxwell-Boltzmann (sampled Gaussian) distribution is considered, and the SNRs are computed using the GN model. In [8], the EGN model is adopted, and the kurtosis-dependence of the NLI is used to explain the reason why AWGN-optimal shaping strategies have an SNR-penalty with respect to uniform signaling: the Gaussian distribution has a relatively high kurtosis. Results in [19] experimentally confirmed this kurtosis-dependence for single-span links. The results in [19] also show that gains obtained by optimizing inputs specifically for optical channels exist, but are limited.

In [20], the input distribution is optimized for a 16-ary constellation using the EGN model and assuming the NLI is circularly symmetric AWGN. It is concluded that AWGN-optimal inputs are good enough. However, there are two caveats here: First, as found in [17] and stated in [20], the kurtosis has the greatest influence for short links. On the other hand in [20, Fig. 2], it is not possible to evaluate the effect of kurtosis for short distances since the span length is taken to be 80 km, and when the number of spans is below 15, all considered schemes have mutual information (MI) converging to  $\log_2 16 = 4$  bit per symbol, i.e., the optimum distribution converges to uniform. Second, the MI is estimated assuming that the NLI noise is circularly symmetric Gaussian. However, for short distances (especially for single-span links), this is not the case [15, Fig. 1].

In [21], optimized input distributions are computed taking into account the effect of kurtosis, and gains in achievable information rates (AIRs)—although small—are observed for 256- and 1024-ary constellations. Unlike [20], a single-span 200 km link is considered in which the effect of kurtosis is expected to be significant and the NLI noise is not circularly

Y. C. Gültekin, A. Alvarado and F. M. J. Willems are with the Information and Communication Theory Lab, Signal Processing Systems Group, Department of Electrical Engineering, Eindhoven University of Technology, Eindhoven 5600 MB, The Netherlands (e-mails: {y.c.g.gultekin, a.alvarado, f.m.j.willems}@tue.nl).

C. M. Okonkwo is with the Electro-Optical Communications Group, Institute for Photonics Integration, Department of Electrical Engineering, Eindhoven University of Technology, Eindhoven 5600 MB, The Netherlands (e-mail: cokonkwo@tue.nl).

O. Vassilieva, I. Kim and P. Palacharla are with the Fujitsu Network Communications, Inc., Richardson, 75082 TX, USA (e-mails: {olga.vassilieva, inwoong.kim}@us.fujitsu.com).

The work of Y. C. Gültekin and A. Alvarado has received funding from the European Research Council (ERC) under the European Union's Horizon 2020 research and innovation programme (grant agreement No 57791).

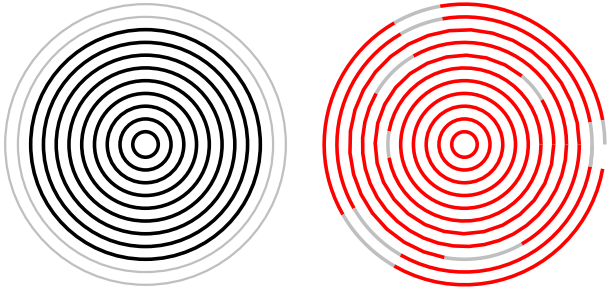


Fig. 1. Illustration of the shell occupation in an  $N$ -dimensional sphere for (left) sphere shaping and (right) kurtosis-limited sphere shaping. Due to the limit on kurtosis, some sequences in the sphere are left out of the shaping set. Since a higher energy usually implies a higher kurtosis, removed sequences are mostly from outermost shells. To compensate for the decrease in number of sequences, i.e., rate, this causes, additional shells are included. We note that similar illustrations are shown in [6, Fig. 1], [25, Fig. 6], and [7, Fig. 2].

symmetric Gaussian. However, the study is limited to AIR computations, and no shaping algorithm is implemented.

In [22], a shaping technique, namely hierarchical distribution matching [23], [24], is discussed. The implementation of this technique is based on lookup tables (LUTs). In [22, Sec. IV], these LUTs are generated such that channel input sequences that have higher  $j^{\text{th}}$  order moments are discarded for  $j \leq 8$ . It is concluded that for systems where the dominant source of impairment is the noise generated by the amplifiers, considering only the second order moment is optimum. However for short links, optimizing higher order moments improves the performance [22, Fig. 4]. A concise review of some of the other works attempting to use non-AWGN-optimal distributions to decrease NLI can be found in [19, Sec. I].

Although it is well recognized in the literature that kurtosis is important in NLI generation, no constructive algorithms exist implementing specifically kurtosis-limited shaping. Here, we attempt to provide such an algorithm using an “indirect” method according to the terminology of [26]: by changing the bounding geometry of the signal space, rather than trying to obtain a target input distribution. Spherical signal structures (as illustrated in 1 (left)) are optimum for the AWGN channel [27]. However, other bounding geometries may lead to more efficient signal sets for non-AWGN channels as we discussed in [25, Sec. I]. With this motivation, in this work:

- 1) We introduce a new amplitude shaping approach which we call kurtosis-limited sphere shaping (KLSS). KLSS extends the idea of sphere shaping, which is to construct a spherical signal space to obtain an input with Gaussian-like distribution, by imposing a constraint on the kurtosis of the signal points. With this additional constraint, we effectively propose to use a non-spherical signal structure for optical channels as illustrated in Fig. 1 (right).
- 2) We show that KLSS generates signal sets with slightly higher average energy than that of sphere shaping, but with a smaller average kurtosis.
- 3) We implement a KLSS-based amplitude shaper using a modified version of the enumerative sphere shaping (ESS) algorithm [6], [28]. This new algorithm, i.e., K-

ESS, creates an invertible mapping from binary indices to amplitude sequences within the KLSS set.

Simulation results show that PAS with K-ESS recovers some of the SNR-penalty observed with AWGN-optimal ESS for single-span links. End-to-end decoding results demonstrate that with KLSS, smaller frame error rates (FERs) than sphere shaping and uniform signaling are obtained. ESS can be recovered as a special case of K-ESS, and thus, K-ESS generalizes ESS.

The remainder of the paper is organized as follows. In Sec. II, some background information is provided, and the system model is described. In Sec. III, KLSS and K-ESS are introduced. Numeric results are then discussed in Sec. IV. And finally, some conclusions are drawn in Sec. V.

## II. SYSTEM MODEL & PROBLEM STATEMENT

### A. Probabilistic Amplitude Shaping

In this study, we restrict our attention to probabilistic amplitude shaping (PAS) [2]. PAS is a layered coded modulation strategy where in the first layer, an amplitude shaper determines the amplitudes  $a^n = (a_1, a_2, \dots, a_n)$  of the channel inputs. In the second layer, a forward error correction (FEC) code is used to encode these amplitudes to obtain the corresponding signs  $s^n \in \{-1, +1\}^n$  in the form of parity bits. Typically, this is achieved by using a systematic FEC code. Assuming that the FEC encoding produces uniform signs [2, Sec. IV-A2], the channel input distribution and the properties of the channel input sequences are determined by the amplitude shaper.

### B. Amplitude Shaping for the AWGN Channel

The capacity of the average-power-constrained AWGN channel can be achieved when the input  $X$  is a zero-mean, independent and identically distributed Gaussian. Corresponding input sequences  $x^n = (x_1, x_2, \dots, x_n)$  can be shown to be confined in an  $n$ -sphere for  $n$  large enough. Reciprocally, it is possible to show that if the signal space is bounded by an  $n$ -sphere, lower-dimensional input distributions converge to a Gaussian for  $n$  large enough. Motivated by this duality, there are two main approaches to realize amplitude shaping in the PAS framework for the AWGN channel. The first, is to try to obtain a sampled Gaussian (Maxwell-Boltzmann, MB) distribution at the output of the amplitude shaper by using distribution matching. Distribution matching can be based on constant compositions [3], multiset-partitions [4], etc. The second approach is to try to obtain a spherically-constrained signal space by using sphere shaping, e.g., via shell mapping [5], enumerative sphere shaping (ESS) [6], Huffman-coded sphere shaping [7], etc. In this work, we focus on the second approach via ESS and refer the reader to [25] for a comparison of distribution matching and sphere shaping. Sphere shaping considers the energy-constrained amplitude sequences in the set

$$\mathcal{A}^\bullet = \left\{ a^N : \sum_{i=1}^N a_i^2 \leq E^\bullet \right\}, \quad (1)$$

where  $a_i \in \mathcal{A} = \{1, 3, \dots, M-1\}$  for  $i = 1, 2, \dots, N$ , and  $M = 2^m$  for a positive integer  $m$ . The set  $\mathcal{A}$  is the amplitude alphabet of  $M$ -ary amplitude-shift keying ( $M$ -ASK) and of the real and imaginary parts of  $M^2$ -ary quadrature amplitude modulation ( $M^2$ -QAM). There are  $|\mathcal{A}^\bullet|$  amplitude sequences in  $\mathcal{A}^\bullet$ , and the input length of an amplitude shaper that outputs  $a^N \in \mathcal{A}^\bullet$  is defined as  $k = \lfloor \log_2 |\mathcal{A}^\bullet| \rfloor$  bits. In (1),  $E^\bullet$  is the maximum energy that the signal points are allowed to have, i.e., the squared radius of the  $N$ -sphere. By changing the value of  $E^\bullet$ , the shaping rate  $k/N$  can be adjusted.

### C. Amplitude Shaping for the Optical Channel

In [14], the effective SNR of an optical signal after propagation is defined as  $\text{SNR}_{\text{eff}} \triangleq P_{\text{tx}}/(\sigma_{\text{ASE}}^2 + \sigma_{\text{NLI}}^2)$  where  $P_{\text{tx}}$  is the optical launch power,  $\sigma_{\text{ASE}}^2$  is the variance of the noise introduced by the amplifiers, and  $\sigma_{\text{NLI}}^2$  is the variance of the NLI. In the GN model of [14], the NLI is modeled as a circularly symmetric Gaussian noise whose properties are assumed to be independent of the input modulation format and distribution. This assumption was later shown to be inaccurate, and the EGN model was proposed [15], [16].

The  $k^{\text{th}}$  order standardized moment is defined as [8, eq. (19)]

$$\begin{aligned} \mu_k &= \frac{E[|X - E[X]|^k]}{(E[|X - E[X]|^2])^{\frac{k}{2}}} \\ &= E[|X|^k], \end{aligned} \quad (2)$$

for a channel input  $X$  that is symmetric around the origin and has unit energy. The EGN model shows that the variance  $\sigma_{\text{NLI}}^2$  of NLI can be expressed as [8, eq. (17)]

$$\sigma_{\text{NLI}}^2 = P_{\text{tx}}^3 [\chi_0 + (\mu_4 - 2)\chi_4 + (\mu_4 - 2)^2\chi'_4 + \mu_6\chi_6]. \quad (3)$$

In (3),  $\chi_0, \chi_4, \chi'_4$ , and  $\chi_6$  are coefficients that are determined by fiber parameters. Considering that  $\chi'_4$  is typically negative, and that  $\mu_4$  is typically smaller than 2, (3) implies that as  $\mu_4$  or  $\mu_6$  increases, the NLI variance increases as well [8]. Consequently, the SNR-penalty observed for AWGN-optimal input distributions in [8, Sec. IV-E1] is explained by the higher kurtosis values of such distributions [8, Table II].

As an example in Fig. 2, we plotted the kurtosis of the channel input  $X$  with amplitudes selected with sphere shaping. As the distribution is shaped more, i.e., as  $E^\bullet$ ,  $k/n$  and  $H(X)$  all decrease, kurtosis increases and then decreases for small rates. Furthermore, when the shaping redundancy is around 1 bit, the kurtosis is very close to the maximum possible, i.e., to that of a continuous Gaussian. We conclude from Fig. 2 that finite-blocklength sphere shaping leads to input distributions with high kurtosis which increases NLI variance, and accordingly, decreases effective SNR. However, the increase in AIRs due to shaping is larger, and a positive net gain is obtained, especially for long-haul transmission [8, Sec. IV-E]. In the next section, we will propose a new sphere shaping approach to lower the kurtosis, and thus, recover the SNR-penalty.

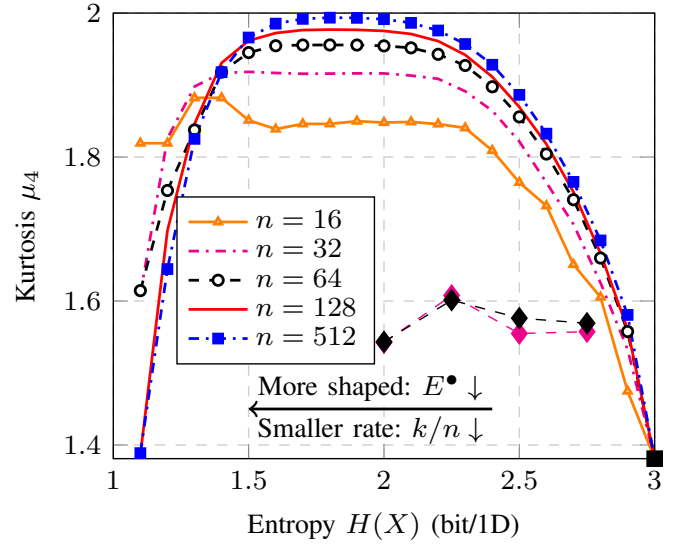


Fig. 2. Kurtosis  $\mu_4$  of the channel inputs obtained using sphere shaping with 64-QAM. Black square corresponds to uniform 64-QAM with kurtosis 1.381 [8, Table II]. For uniform phase-shift keying constellations, kurtosis is equal to 1. The diamonds correspond to KLSS.

## III. KURTOSIS-LIMITED SPHERE SHAPING

### A. Kurtosis Constraint on Amplitude Sequences

We want to devise a shaping technique that has smaller kurtosis than that of sphere shaping. Consider the energy- and kurtosis-constrained amplitude sequences in the set

$$\mathcal{A}^\bullet = \left\{ a^N : \sum_{i=1}^N a_i^2 \leq E^\bullet \text{ and } \sum_{i=1}^N a_i^4 \leq K^\bullet \right\}. \quad (4)$$

We call this set the kurtosis-limited sphere shaping (KLSS) set. Similar to sphere shaping, the input length of an amplitude shaper that outputs  $a^N \in \mathcal{A}^\bullet$  is defined as  $k = \lfloor \log_2 |\mathcal{A}^\bullet| \rfloor$  bits. The shaping rate  $k/N$  can be adjusted by changing the values of  $E^\bullet$  and  $K^\bullet$ . As  $K^\bullet$  decreases, sequences with high kurtosis are eliminated from the shaping set, and hence, the rate decreases. As  $K^\bullet \rightarrow \infty$ ,  $\mathcal{A}^\bullet$  converges to the regular sphere shaping set  $\mathcal{A}^\bullet$  in (1).

In Fig. 2, the minimum  $\mu_4$  value that can be obtained with KLSS is also shown (diamond markers). We see that the kurtosis-limitation indeed leads to smaller  $\mu_4$  than that of sphere shaping at the same rate. Furthermore,  $\mu_4$  is relatively flat and roughly independent of  $N$  for KLSS.

Figure 3 demonstrates the effect of the kurtosis constraint  $K^\bullet$ . Three cases are considered: Blue histogram belongs to sphere shaping, i.e., only  $E^\bullet$  is finite. Red histogram belongs to KLSS, i.e., both  $E^\bullet$  and  $K^\bullet$  are finite. Green histogram belongs to the other extreme where only  $K^\bullet$  is finite. The shaping rate is  $k/N = 1.5$  bits per amplitude (bit/amplitude), which can be achieved by increasing  $E^\bullet$  for decreasing values of  $K^\bullet$ . The trend to have more sequences with smaller kurtosis as  $K^\bullet$  decreases is self evident in Fig. 3.

The effect of changing  $E^\bullet$  and/or  $K^\bullet$  can be visualized as in the inset figure of Fig. 3 where we show the  $E^\bullet K^\bullet$ -plane. For each point on this plane, the corresponding set  $\mathcal{A}^\bullet$  (4) can

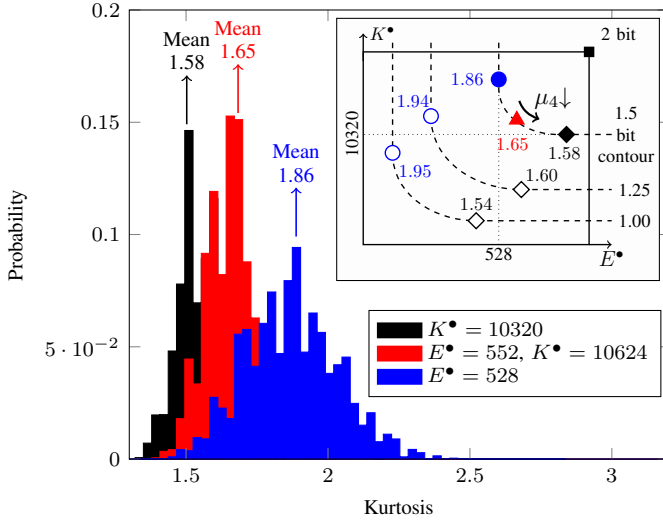


Fig. 3. Histograms of kurtosis of sequences for  $N = 64$  with 64-QAM. Kurtosis of a sequence  $a^N$  is computed using (2) with the corresponding empirical distribution. The inset figure shows the  $E^*K^*$ -plane with  $k/N = 1.00, 1.25$  and  $1.50$  bit/amplitude shaping rate contours. Here, black square effectively represents uniform signaling where there is no constraint on energy or kurtosis, i.e., a cubical signal space.

be found. The filled blue circle corresponds to sphere shaping with only an energy constraint, i.e.,  $E^* = 796$ . On the other hand, the filled black diamond represents the case with only a kurtosis constraint, i.e.,  $K^* = 15444$ . The curve that connects these points is the contour line of constant shaping rate  $k/N = 1.50$  bit/amplitude. On this curve, as we move away from sphere shaping, kurtosis decreases, however average energy increases. We have also illustrated the contour lines of  $1.25$  and  $1.00$  bit/amplitude.

Figure 4 shows the trade-off between average energy  $\sum_{a \in \mathcal{A}} p(a)a^2$  and kurtosis when moving on a constant shaping rate contour. As  $E^*$  increases, the average energy per symbol increases. At the same time,  $K^*$  decreases leading to a decrease in kurtosis. We also see from Fig. 4 that after approximately  $E^* = 584$  ( $K^* = 10320$ ), increasing  $E^*$  only has marginal effect. This is because the proportion of sequences that have energy larger than 584 and kurtosis smaller than 10320 that are included in the shaping set is extremely small.

### B. Enumerative Sphere Shaping

Enumerative sphere shaping (ESS) is an algorithm to index amplitude sequences in an  $N$ -sphere  $a^N \in \mathcal{A}^*$  [6], [28]. To realize ESS, first an enumerative amplitude trellis is generated, as shown in Fig. 5 for  $N = 3$ ,  $\mathcal{A} = \{1, 3, 5\}$  and  $E^* = 27$ . Here, nodes in the  $n^{\text{th}}$  column represent the accumulated energy of the sequences for their first  $n$  amplitudes, more precisely,  $\sum_{i=1}^n a_i^2$ . The nodes are labeled with the energy level ( $e$ ) that they represent. Color-coded branches that connect a node in  $(n-1)^{\text{th}}$  column to a node in  $n^{\text{th}}$  column represent  $a_n$ . Each 3-amplitude sequence is shown by a 3-branch path that starts at node (0) and ends in a node in the final (rightmost) column. Possible values for sequence energy are 3, 11, 19 and 27. As an example, the path that corresponds to  $(3, 3, 3)$  with

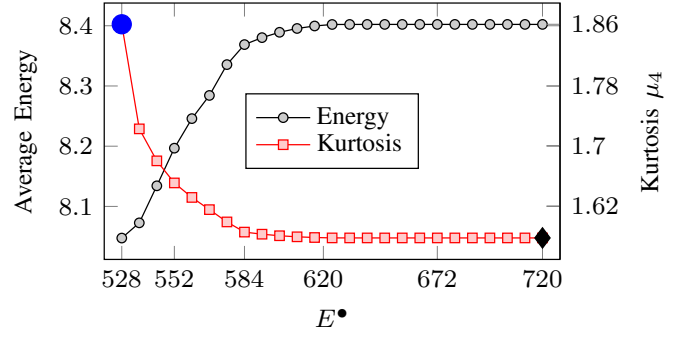


Fig. 4. Trade-off between the average energy per symbol and kurtosis  $\mu_4 = E[|X|^4]$  for the pairs of  $E^*$  and  $K^*$  on the  $1.5$  bit/amplitude shaping rate contour in the inset of Fig. 3. The black diamond corresponds to the kurtosis-limited scheme in Fig. 2 and in the inset of Fig. 3. The blue circle corresponds to the energy-limited scheme in the inset of Fig. 3.

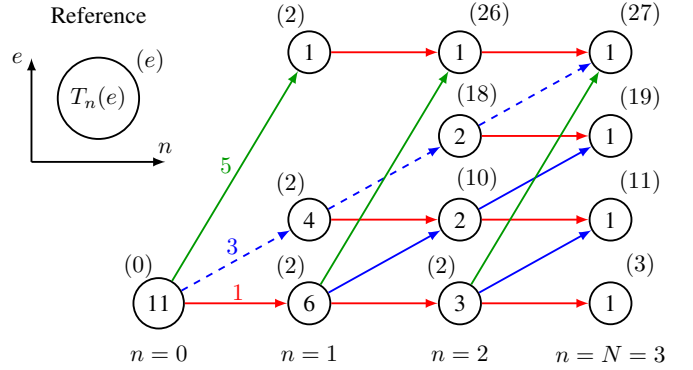


Fig. 5. Bounded-energy enumerative amplitude trellis for  $\mathcal{A} = \{1, 3, 5\}$ ,  $N = 3$  and  $E^* = 28$ .

energy 27 is drawn with dashed lines in Fig. 5. The values written inside each node are computed using

$$T_n(e) \triangleq \sum_{a \in \mathcal{A}} T_{n+1}(e + a^2), \quad (5)$$

for  $n = 0, 1, \dots, N-1$  where the initialization is as follows:

$$T_N(e) = \begin{cases} 1 & : e \leq E^*, \\ 0 & : \text{otherwise} \end{cases} \quad (6)$$

In (5),  $T_n(e)$  is the number of ways to reach a final node starting from the node of energy  $e$  in the  $n^{\text{th}}$  column. Thus,  $T_0(0)$  gives the number of sequences  $|\mathcal{A}^*|$  represented in the trellis, which is 11 in Fig. 5. This means there are 11 3-amplitude sequences with energy no greater than 27. Note that only the accumulated energy values that can possibly occur are considered in Fig. 5. Based on this enumerative trellis, ESS realizes a lexicographical mapping from indices, i.e.,  $\lfloor \log_2 T_0(0) \rfloor = k$ -bit strings, to amplitude sequences in  $\mathcal{A}^*$  [6, Sec. III-C].

### C. KLSS Implementation Based on ESS

To realize a kurtosis-limited sphere shaping (KLSS), we introduce a modified version of the enumerative amplitude trellis explained in the previous section. We again use an example trellis shown in Fig. 6 for the same set of parameters



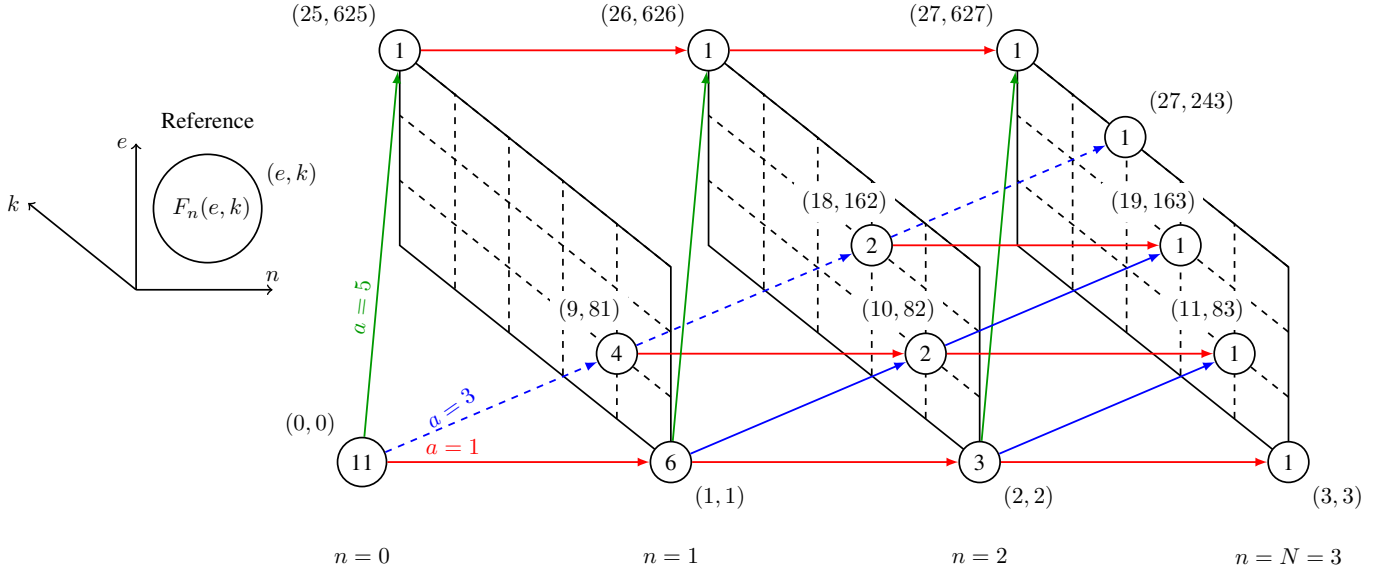


Fig. 6. Bounded-energy and bounded-kurtosis enumerative amplitude trellis for  $\mathcal{A} = \{1, 3, 5\}$ ,  $N = 3$ ,  $E^\bullet = 28$  and  $K^\bullet = 627$ .

as Fig. 5 and  $K^\bullet = 627$ . Now, nodes in the  $n^{\text{th}}$  plane represent the accumulated energy and the accumulated kurtosis  $\sum_{i=1}^n a_i^4$  of the sequences for their first  $n$  amplitudes. The nodes are labeled with the energy-kurtosis pair  $(e, k)$  that they represent. Similar to Fig. 5, each 3-amplitude sequence is shown by a 3-branch path that starts at node  $(0, 0)$  and ends in a node in the final (rightmost) plane. Possible values for sequence energy-kurtosis pairs are  $(3, 3)$ ,  $(11, 83)$ ,  $(19, 163)$ ,  $(27, 243)$  and  $(27, 627)$ . Again the path that corresponds to  $(3, 3, 3)$  with energy 27 and kurtosis 243 is drawn with dashed lines in Fig. 6.

Similar to (5), the values written inside each node are computed using

$$F_n(e, k) \triangleq \sum_{a \in \mathcal{A}} F_{n+1}(e + a^2, k + a^4), \quad (7)$$

for  $n = 0, 1, \dots, N-1$  where the initialization is as follows:

$$F_N(e, k) = \begin{cases} 1 & : e \leq E^\bullet \text{ and } k \leq K^\bullet, \\ 0 & : \text{otherwise} \end{cases} \quad (8)$$

In (7),  $F_n(e, k)$  is the number of ways to reach a final node starting from the node of energy  $e$  and kurtosis  $k$  in the  $n^{\text{th}}$  plane. Accordingly,  $F_0(0, 0) = |\mathcal{A}^\bullet|$  is the number of sequences represented in the trellis. Note that when you look to the trellis in Fig. 6 from the  $en$ -plane, the trellis in Fig. 5 is seen. The difference is that now, we have control also on the maximum value of kurtosis allowed in the trellis. As an example, in the maximum-energy-bounded trellis of Fig. 5, when the final node of energy 27 is included, all sequences with energy 27 are in the shaping set:  $(1, 1, 5)$ ,  $(1, 5, 1)$ ,  $(3, 3, 3)$  and  $(5, 1, 1)$ . However, in the maximum-energy- and maximum-kurtosis-bounded trellis of Fig. 6, it is possible to include the final node  $(27, 243)$  while excluding  $(27, 627)$ . This way,  $(1, 1, 5)$ ,  $(1, 5, 1)$  and  $(5, 1, 1)$  can be left out, while  $(3, 3, 3)$  stays in, which leads to a decrease in  $\mu_4$ .

Finally, the enumerative encoding and decoding algorithms explained in [6, Sec. III-C] can be used also based on  $F(e, k)$

to create an invertible mapping from  $\lfloor \log_2 F(0, 0) \rfloor = k$ -bit indices to sequences in  $\mathcal{A}^\bullet$ . We call this kurtosis-limited ESS (K-ESS), and we note that low-complexity implementation techniques introduced for ESS in [29] can be applied to K-ESS straightforwardly. It is important to note that in (8), we only consider the pairs of  $(e, k)$  in the  $N^{\text{th}}$  (final) plane that can possibly occur for an  $N$ -tuple of amplitudes. We determine these pairs of energy and kurtosis by an exhaustive search over all possible compositions of amplitudes. This is different than ESS in which the corresponding initialization is done by setting  $T_N^e = 1$  for all  $e \leq E^\bullet$  [6, Sec. III-B].

In the next section, we will simulate PAS with K-ESS to check whether we can recover the SNR-penalty observed for AWGN-optimal channel inputs due to their high kurtosis.

## IV. NUMERIC RESULTS

### A. Performance Improvement by K-ESS

To demonstrate the effectiveness of KLSS, we simulated single-channel transmission over a single span of 205 km standard single-mode optical fiber (SSMF) with an attenuation of 0.2 dB/km, a dispersion parameter of 17 ps/nm/km and a nonlinear parameter of 1.3 1/W/km, followed by an erbium doped amplifier with a noise figure of 5 dB. The propagation of the optical field over the SSMF is simulated using the split-step Fourier method based on the nonlinear Schrödinger and Manakov equations for SP and DP transmission, respectively.

The transmitter generates a single- or a dual-polarized (SP or DP) 50 GBd signal using 64-QAM constellation. In the DP case, the transmission rate is 8 bit/4D symbol, yielding a raw data rate of 600 Gbit/s. The target is a net data rate of 400 Gbit/s. With uniform signaling, this rate is obtained using a rate 2/3 channel code. With PAS, we use a rate 5/6 channel code with an amplitude shaper with rate 1.5 bit/amplitude. How these shaping and coding rates lead to a transmission rate of 2 bit/1D symbol is explained in [30, Footnote 1]. The channel codes used are the low-density parity-check (LDPC)

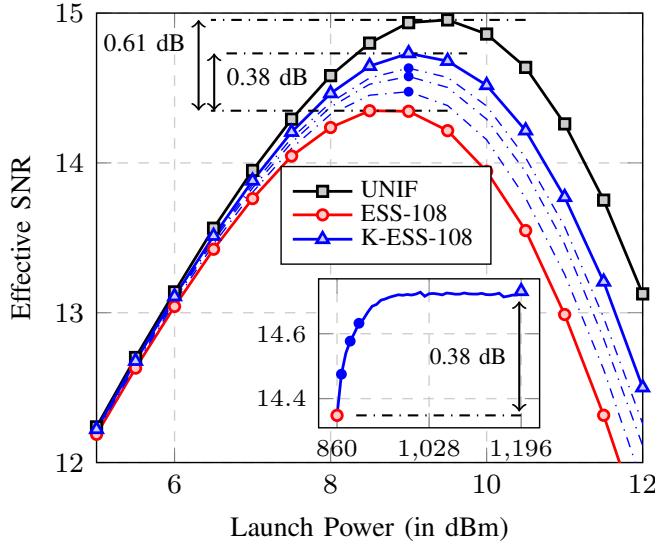


Fig. 7. Effective SNR vs. launch power for the transmission of 200 Gbit/s SP-64-QAM over a 213-km-long SSMF. **Inset:** Effective SNR at the optimum launch power as a function of  $E^\bullet$  of the K-ESS trellis. Optimum power is 9 dBm for all considered K-ESS schemes. Red circle represents regular sphere shaping. Blue circles represents the K-ESS trellises for which the launch power vs. effective SNR performance is shown with the dash-dotted curves in the outer figure.

codes of the IEEE 802.11 standard with a codeword length of 648 bits [31]. We consider both ESS and K-ESS with  $n = 108$ . There is a single ESS trellis that satisfies the 1.5 bit/amplitude shaping rate constraint, with  $E^\bullet = 860$ . On the other hand, there are 42  $(E^\bullet, K^\bullet)$  pairs that lead to a KLSS set (4) with a shaping rate of 1.5 bit/amplitude.

For the mapping of coded bits to QAM symbols, the binary reflected Gray code is used [32, Defn. 2.10]. For the mapping of amplitudes to QAM symbols, the 4D mapping strategy illustrated in [33, Fig. 3(c)] is used. More precisely, a shaped amplitude sequence of length  $N$  is mapped to a 4D symbol sequence of length  $N/4$ , or equivalently, four consecutive shaped amplitudes are mapped to four concurrent quadratures. Note that in the SP case, this corresponds to the 2D mapping strategy of [33, Fig. 3(b)].

Figures 7 and 8 show the effective SNR as a function of optical launch power for SP and DP transmission, respectively. We see that due to its high kurtosis, ESS has an SNR-penalty with respect to uniform signaling. The penalty is slightly higher in the case of SP transmission, i.e., 0.58 dB instead of 0.41 dB. This is in agreement with [15, Sec. 5] where it is discussed that the effect of kurtosis on NLI variance is slightly more significant for SP transmission. Figures 7 and 8 show that K-ESS recovers some of this SNR-loss thanks to its smaller kurtosis. Another observation from the effective SNR curves is that the optimum launch power for K-ESS is larger than that of ESS for both SP and DP transmission, and is the same as that of uniform signaling in DP case. This also implies that K-ESS is able to recover some of the nonlinearity tolerance that is lost when ESS is employed instead of uniform transmission.

In Fig. 7, we show the effective SNR for 4 out of the 42 available K-ESS trellises at the considered rate, i.e., as the

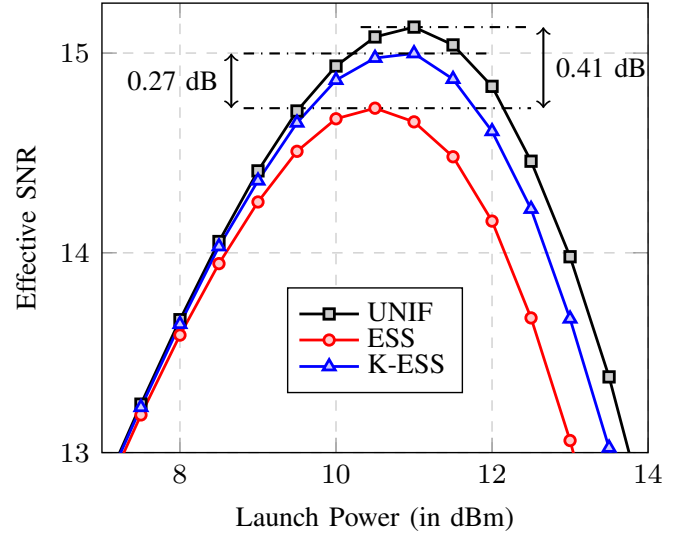


Fig. 8. Effective SNR vs. launch power for the transmission of 400 Gbit/s DP-64-QAM over a 205-km-long SSMF.

operating point moves on the 1.5 bit shaping rate contour away from regular sphere shaping, similar to the inset figure of Fig. 3. This clearly demonstrates that as  $E^\bullet$  increases and  $K^\bullet$  decreases, the decrease in kurtosis  $\mu_4$  results in an improvement in effective SNR. In the inset figure, this trend is shown by plotting the effective SNR at the optimum launch power<sup>1</sup> as a function of  $E^\bullet$ . We see that as  $E^\bullet$  increases and  $\mu_4$  decreases, effective SNR increases and converges to 15.82 dB. This behavior is consistent with the convergence observed for average energy and kurtosis in Fig. 4.<sup>2</sup> The outermost K-ESS curve in Fig. 7 (triangular markers) has the maximum effective SNR and is considered to be the “best” trellis for this setup. We note that the “best” trellis may change depending on the parameters of the optical link and the communication scenario such as the number of channels and the bandwidth. Furthermore, for the same setup, the trellis that maximizes the SNR and the one that minimizes the FER might differ. In Fig. 8 and Fig. 10, we therefore only plot the curve that belongs to the K-ESS trellis that optimizes the corresponding performance metric.

Figures 9 and 10 show the FER as a function of optical launch power for SP and DP transmission, respectively. We see that although ESS had an SNR-penalty because of its high kurtosis with respect to uniform signaling (see Figs. 7 and 8), the net gain (combined with the improvement in AIRs that results from shaping) in FERs is positive for DP transmission. This is as observed in [8, Sec. IV-E]. For SP transmission, the SNR-penalty and shaping gain cancel each other out. In both SP and DP cases, ESS achieves the minimum FER at a smaller optimum launch power than uniform signaling. This indicates that ESS has a decreased nonlinearity tolerance, but still a

<sup>1</sup>The term “optimum launch power” is the value at which the corresponding effective SNR or FER curve has its maximum.

<sup>2</sup>It is found in [15], [16] that the sixth order moment also plays a (relatively insignificant) role in NLI generation. For the sake of completeness, we report here that the sixth order moment  $\mu_6$  also exhibits a convergence behavior for KLSS, similar to the one that is shown in Fig. 4 for kurtosis.

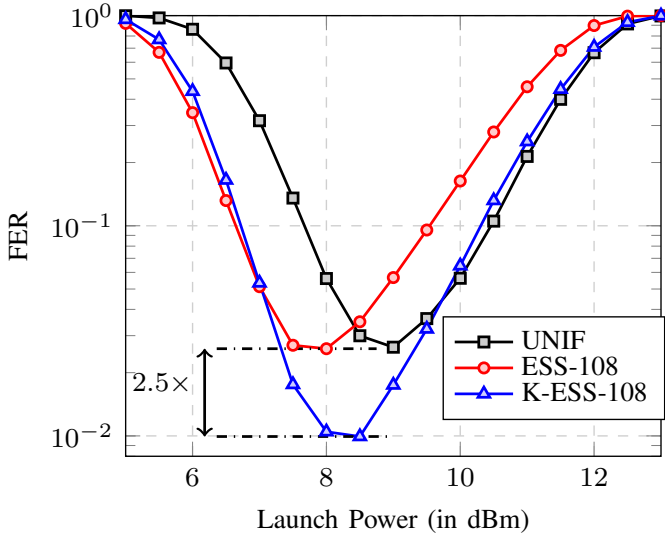


Fig. 9. FER vs. launch power for the transmission of 200 Gbit/s SP-64-QAM over a 213-km-long SSF.

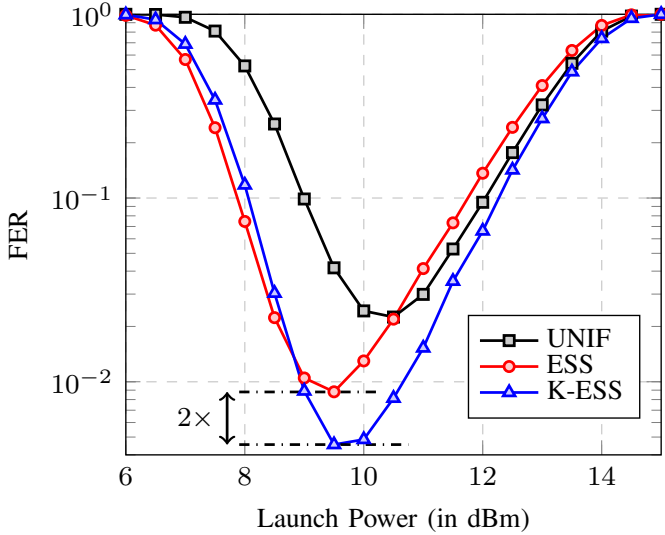


Fig. 10. FER vs. launch power for the transmission of 400 Gbit/s DP-64-QAM over a 205-km-long SSF.

decoding performance either as good as uniform signaling (SP), or better (DP). With K-ESS, it is possible to obtain a better position at this trade-off. We see that K-ESS further decreases the FERs by at least twofold with respect to ESS, while increasing the optimum launch power. This is thanks to the optimized trade-off between the nonlinearity tolerance (due to decreased kurtosis) and the shaping gain in AIR provided by K-ESS.

### B. Rate Adaptivity

To investigate the performance of K-ESS at different transmission rates, we also simulated single-channel transmission over a single span of 227 km SSF at a rate of 6 bit/4D symbol. The transmitter generates a DP 50 GBd signal again using 64-QAM leading to 300 Gbit/s net data rate. With

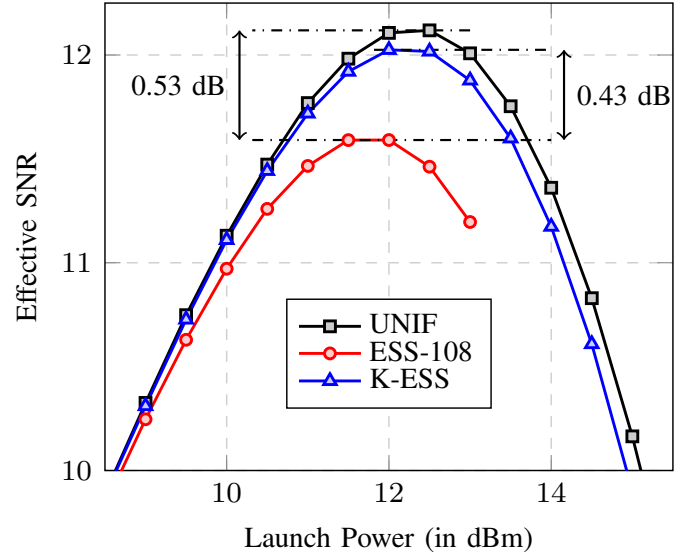


Fig. 11. Effective SNR vs. launch power for the transmission of 300 Gbit/s DP-64-QAM over a 227-km-long SSF.

uniform signaling, this rate is obtained using a rate 1.2 channel code. With PAS, we again use a rate 5/6 channel code, now with an amplitude shaper with rate 1 bit/amplitude. We consider both ESS and K-ESS with  $n = 108$ . The ESS trellis that satisfies 1 bit/amplitude rate is with  $E^* = 428$ . However there are 9  $(E^*, K^*)$  pairs that lead to a KLSS set (4) with rate 1 bit/amplitude.

Figures 11 and 12 show the effective SNR and FER as a function of launch power for the 300 Gbit/s transmission, respectively. We see that the improvements provided by K-ESS over ESS in effective SNR (0.43 dB) and FER (5 times) at the optimum launch power are larger than their counterparts in the 400 Gbit/s case. This is because at this shaping rate of 1 bit/amplitude ( $H(X) \approx 2$  bit/1D symbol) the decrease in kurtosis obtained using KLSS instead of regular sphere shaping is larger than that of 1.5 bit/amplitude ( $H(X) \approx 2.5$  bit/1D symbol), as seen in Fig. 2. Therefore, we claim that the performance of K-ESS relative to ESS can be predicted considering the corresponding values of kurtosis, and Fig. 2 suggests that the largest improvement can be expected for shaping rates between 0.5 and 1.5 bit/amplitude for 64-QAM.

## V. CONCLUSIONS

We proposed kurtosis-limited sphere shaping (KLSS) as a constellation shaping technique tailored for optical channels. KLSS creates channel input distributions with a smaller fourth order moment (i.e., kurtosis) than that of Gaussian-channel-optimized inputs. Shaped inputs with smaller kurtosis can be used to improve the trade-off between (1) the increased nonlinear interference due to higher kurtosis, and (2) the increased shaping gain due to smaller average energy. KLSS is implemented using a modified version of the enumerative sphere shaping algorithm. Simulations of transmission over SSF demonstrate that KLSS is able to recover most of

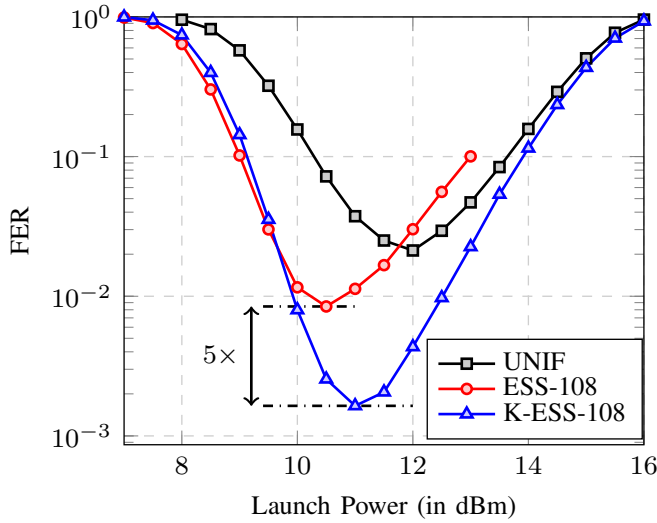


Fig. 12. FER vs. launch power for the transmission of 300 Gbit/s DP-64-QAM over a 227-km-long SSF.

the effective SNR-penalty experienced with Gaussian-channel-optimized inputs. End-to-end decoding results show that smaller frame error probabilities can be achieved with KLSS. Future work should focus on evaluating the performance of KLSS in different optical communication scenarios such as multi-channel and multi-span transmission at different shaping blocklengths and higher-order constellations.

## REFERENCES

- [1] T. M. Cover and J. A. Thomas, *Elements of Information Theory*, 2nd ed. Hoboken, NJ, USA: John Wiley & Sons, 2006.
- [2] G. Böcherer, F. Steiner, and P. Schulte, "Bandwidth efficient and rate-matched low-density parity-check coded modulation," *IEEE Trans. Commun.*, vol. 63, no. 12, pp. 4651–4665, Dec. 2015.
- [3] P. Schulte and G. Böcherer, "Constant composition distribution matching," *IEEE Trans. Inf. Theory*, vol. 62, no. 1, pp. 430–434, Jan. 2016.
- [4] T. Fehenberger, D. S. Millar, T. Koike-Akino, K. Kojima, and K. Parsons, "Multiset-partition distribution matching," *IEEE Trans. Commun.*, vol. 67, no. 3, pp. 1885–1893, Mar. 2019.
- [5] P. Schulte and F. Steiner, "Divergence-optimal fixed-to-fixed length distribution matching with shell mapping," *IEEE Wireless Commun. Lett.*, vol. 8, no. 2, pp. 620–623, Apr. 2019.
- [6] Y. C. Gültekin, W. J. van Houtum, A. Koppelaar, and F. M. J. Willems, "Enumerative sphere shaping for wireless communications with short packets," *IEEE Trans. Wireless Commun.*, vol. 19, no. 2, pp. 1098–1112, Feb. 2020.
- [7] T. Fehenberger, D. S. Millar, T. Koike-Akino, K. Kojima, K. Parsons, and H. Griesser, "Huffman-coded sphere shaping and distribution matching algorithms via lookup tables," *J. Lightw. Technol.*, vol. 38, no. 10, pp. 2826–2834, May 2020.
- [8] T. Fehenberger, A. Alvarado, G. Böcherer, and N. Hanik, "On probabilistic shaping of QAM for the nonlinear fiber channel," *J. Lightw. Technol.*, vol. 34, no. 21, pp. 5063–5073, Nov. 2016.
- [9] F. Buchali, F. Steiner, G. Böcherer, L. Schmalen, P. Schulte, and W. Idler, "Rate adaptation and reach increase by probabilistically shaped 64-QAM: An experimental demonstration," *J. Lightw. Technol.*, vol. 34, no. 7, pp. 1599–1609, Apr. 2016.
- [10] W. Idler *et al.*, "Field trial of a 1 Tb/s super-channel network using probabilistically shaped constellations," *J. Lightw. Technol.*, vol. 35, no. 8, pp. 1399–1406, Apr. 2017.
- [11] S. Goossens *et al.*, "First experimental demonstration of probabilistic enumerative sphere shaping in optical fiber communications," in *Proc. Opto-Electron. and Commun. Conf. and Int. Conf. on Photon. in Switch. and Comput.*, Fukuoka, Japan, July 2019.
- [12] A. Amari *et al.*, "Enumerative sphere shaping for rate adaptation and reach increase in wdm transmission systems," in *Proc. Eur. Conf. Opt. Commun.*, Dublin, Ireland, Sep. 2019.
- [13] —, "Introducing enumerative sphere shaping for optical communication systems with short blocklengths," *J. Lightw. Technol.*, vol. 37, no. 23, pp. 5926–5936, Dec. 2019.
- [14] P. Poggiolini, G. Bosco, A. Carena, V. Curri, Y. Jiang, and F. Forghieri, "The GN-model of fiber non-linear propagation and its applications," *J. Lightw. Technol.*, vol. 32, no. 4, pp. 694–721, Feb. 2014.
- [15] R. Dar, M. Feder, A. Mecozzi, and M. Shtaif, "Properties of nonlinear noise in long, dispersion-uncompensated fiber links," *Opt. Express*, vol. 21, no. 22, pp. 25 685–25 699, Nov. 2013.
- [16] A. Carena, G. Bosco, V. Curri, Y. Jiang, P. Poggiolini, and F. Forghieri, "EGN model of non-linear fiber propagation," *Opt. Express*, vol. 22, no. 13, pp. 16 335–16 362, June 2014.
- [17] R. Dar, M. Feder, A. Mecozzi, and M. Shtaif, "Accumulation of non-linear interference noise in fiber-optic systems," *Opt. Express*, vol. 22, no. 12, pp. 14 199–14 211, June 2014.
- [18] T. Fehenberger, G. Böcherer, A. Alvarado, and N. Hanik, "LDPC coded modulation with probabilistic shaping for optical fiber systems," in *Proc. Opt. Fiber Commun. Conf. (OFC)*, Los Angeles, CA, USA, June 2015.
- [19] J. Renner *et al.*, "Experimental comparison of probabilistic shaping methods for unrepeatable fiber transmission," *J. Lightw. Technol.*, vol. 35, no. 22, pp. 4871–4879, Nov. 2017.
- [20] C. Pan and F. R. Kschischang, "Probabilistic 16-QAM shaping in WDM systems," *J. Lightw. Technol.*, vol. 34, no. 18, pp. 4285–4292, July 2016.
- [21] E. Sillekens *et al.*, "A simple nonlinearity-tailored probabilistic shaping distribution for square QAM," in *Proc. Opt. Fiber Commun. Conf.*, San Diego, CA, USA, Mar. 2018.
- [22] T. Yoshida, E. Agrell, and M. Karlsson, "Hierarchical distribution matching with massively parallel interfaces for fiber-optic communications," in *Proc. Int. Zurich Seminar on Inf. Commun. (IZS)*, Zurich, Switzerland, Feb. 2020, pp. 16–20.
- [23] T. Yoshida, M. Karlsson, and E. Agrell, "Hierarchical distribution matching for probabilistically shaped coded modulation," *J. Lightw. Technol.*, vol. 37, no. 6, pp. 1579–1589, Mar. 2019.
- [24] S. Civielli and M. Secondini, "Hierarchical distribution matching for probabilistic amplitude shaping," *Entropy*, vol. 22, no. 9: 958, Aug. 2020.
- [25] Y. C. Gültekin, T. Fehenberger, A. Alvarado, and F. M. J. Willems, "Probabilistic shaping for finite blocklengths: Distribution matching and sphere shaping," *Entropy*, vol. 19, no. 5: 581, May 2020.
- [26] A. R. Calderbank and L. H. Ozarow, "Nonequiprobable signaling on the Gaussian channel," *IEEE Trans. Inf. Theory*, vol. 36, no. 4, pp. 726–740, July 1990.
- [27] Y. C. Gültekin, W. J. van Houtum, and F. M. J. Willems, "On constellation shaping for short block lengths," in *Proc. Symp. on Inf. Theory and Signal Process. in the Benelux (SITB)*, Enschede, The Netherlands, June 2018, pp. 86–96.
- [28] Y. C. Gültekin, F. M. J. Willems, W. J. van Houtum, and S. Şerbetli, "Approximate enumerative sphere shaping," in *Proc. IEEE Int. Symp. Inf. Theory*, Vail, CO, USA, June 2018, pp. 676–680.
- [29] Y. C. Gültekin, W. J. van Houtum, A. G. C. Koppelaar, and F. M. J. Willems, "Low-complexity enumerative coding techniques with applications to amplitude shaping," *IEEE Commun. Lett.*, vol. 25, no. 1, pp. 33–37, Jan. 2021.
- [30] —, "Comparison and optimization of enumerative coding techniques for amplitude shaping," *IEEE Commun. Lett.*, vol. 25, no. 4, pp. 1231–1235, Apr. 2020.
- [31] *IEEE Std. for Inform. Technol.-Telecommun. and Inform. Exchange Between Syst. LANs and MANs-Part 11: Wireless LAN MAC and PHY Spec.*, IEEE Std. 802.11-2016, Dec. 2016.
- [32] L. Szczecinski and A. Alvarado, *Bit-Interleaved Coded Modulation: Fundamentals, Analysis, and Design*. Chichester, UK: John Wiley & Sons, 2015.
- [33] P. Skvortcov *et al.*, "Huffman-coded sphere shaping for extended-reach single-span links," *IEEE J. Sel. Topics Quantum Electron.*, vol. 27, no. 3: 3500215, May-June 2021.